Title

Microtubules gate tau condensation to spatially regulate microtubule functions.

Journal

Nature cell biology, 21(9)

ISSN

1465-7392

Authors

Tan, Ruensern
Lam, Aileen J
Tan, Tracy
et al.

Publication Date

2019-09-01

DOI

10.1038/s41556-019-0375-5

Peer reviewed

HHS Public Access

Author manuscript

Nat Cell Biol. Author manuscript; available in PMC 2020 March 02.

Published in final edited form as:

Nat Cell Biol. 2019 September ; 21(9): 1078–1085. doi:10.1038/s41556-019-0375-5.

Microtubules Gate Tau Condensation to Spatially Regulate Microtubule Functions

Ruensern Tan[1], **Aileen J. Lam**[1], **Tracy Tan**[1], **Jisoo Han**[2], **Dan W. Nowakowski**[3], **Michael Vershinin**[4], **Sergi Simó**[2], **Kassandra M. Ori-McKenney**[1,*], **Richard J. McKenney**[1,*]

[1]Dept. of Molecular and Cellular Biology. University of California – Davis. 145 Briggs Hall, Davis, CA. 95616.

[2]Dept. of Cell Biology and Human Anatomy, School of Medicine. University of California – Davis. 3402 Tupper Hall, Davis CA. 95616. USA

[3]N Molecular Systems, Inc., Palo Alto, CA. 94303 USA

[4]Dept. of Physics & Astronomy and Biology. University of Utah, Salt Lake City Utah. 84112. USA

Abstract

Tau is an abundant microtubule-associated protein in neurons. Tau aggregation into insoluble fibrils is a hallmark of Alzheimer's disease and other dementias[1], yet the physiological state of tau molecules within cells remains unclear. Using single molecule imaging, we directly observe that the microtubule lattice regulates reversible tau self-association, leading to localized, dynamic condensation of tau molecules on the microtubule surface. Tau condensates form selectively permissible barriers, spatially regulating the activity of microtubule severing enzymes and the movement of molecular motors through their boundaries. We propose that reversible self-association of tau molecules, gated by the microtubule lattice, is an important mechanism of tau's biological functions, and that oligomerization of tau is a common property shared between the physiological and disease forms of the molecule.

Microtubules (MTs) are dynamic, polarized filaments critical for a wide-variety of cellular functions. Highly polarized cells such as neurons rely on the MT cytoskeleton to develop and maintain a specialized cellular architecture. Neurons devote substantial resources towards the regulation of diverse MT-based processes such as polarized active transport by molecular motors, spatial control of MT dynamics, and post-translational modifications of tubulin[2]. Given their central importance, it is not surprising that defects in MT-based pathways often lead to neurodevelopmental or neurodegenerative diseases in humans.

---

*Correspondence to: rjmckenney@ucdavis.edu or kmorimckenney@ucdavis.edu.

Author contributions

R.J.M. and R.T., and K.M.O.-M. conceived of the project. R.T., A.J.L. and T.T. produced reagents. R.T. performed all in vitro experiments. J.H. and S.S. provided hippocampal neuron cultures, D.W.N. created molecular models, M.V. performed data analysis.

Declaration of Interests

Authors declare no financial and non-financial competing interests.

In Alzheimer's disease, the intrinsically disordered MT-associated protein (MAP), tau (*MAPT*), forms insoluble neurofibrillary tangles (NFTs) through aberrant self-association, a process strongly correlated with neuronal death[1]. While tau self-association drives NFT formation in disease, a non-pathological role for the self-association of tau molecules in cells is less clear. Biochemical studies have suggested that tubulin, or MTs, may mediate tau oligomerization[3,4]. Additionally, multivalent interactions between tau molecules can drive liquid-liquid phase separation (LLPS) of tau in solution, promoting aggregation[5-7]. Single molecule studies showed that tau molecules can exist in either static or diffusive populations when bound to MTs, and that tau binds heterogeneously along MTs[8-10]. While these studies reveal diverse molecular behaviors, how these behaviors relate to tau's physiological roles in the cell is unknown.

MT-bound tau has been proposed to regulate the movement of motor proteins. Tau inhibits the anterograde movement of kinesin-1[9,11-13], but its effect on the retrograde movement of cytoplasmic dynein is less clear. High concentrations of tau were reported to reduce dynein's attachment rate to MTs[14], while a non-activated, putative dynein-dynactin co-complex tended to reverse direction upon encountering tau on the MT surface[9]. Tau also regulates the activity of MT severing enzymes, partially blocking the MT-severing activity identified in *Xenopus* egg extracts[15]. Overexpression of tau protects against katanin-, or spastin-induced MT-severing in cells[16,17], while loss of tau in diseased neurons indirectly leads to aberrant spastin activity[18]. Dysfunction of MT-based transport or MT turnover could conceivably explain the neurotoxicity observed in tauopathies, but a cogent molecular mechanism for how tau affects such activities is lacking.

We set out to explore the molecular mechanisms of tau's complex behaviors using in vitro reconstitution with purified components. We directly observed the binding of bacterially-expressed, GFP-tagged full-length (2N4R) human tau (Supplementary Fig. 1a) to taxol-stabilized MTs *in vitro*. Tau molecules initially bound diffusely along the entire MT lattice, followed by the nucleation and expansion of denser regions of molecules that we term "condensates" due to the localized increase in protein density (Figs. 1a-b, Supplementary Video 1). Tau condensates expanded along the MT, with asynchronous, highly variable growth rates from one or both ends of the condensate, and merged with nearby condensates (Figs. 1a-b, Supplementary Fig. 1b). At a fixed total tau concentration, condensate intensity quickly reached a steady state (Fig. 1c). Nucleation of new condensates and further condensate expansion were rarely observed after ten minutes, suggesting the condensation process reached equilibrium in our assay conditions.

Varying the total tau concentration revealed an increase in both condensate frequency and the density of diffusively bound tau surrounding the condensates (Fig. 1d-e). Tau condensates appeared when the total tau concentration was at least 0.25 nM, while only diffuse tau binding was observed at lower concentrations, revealing a critical concentration for condensation in our conditions. Pixel intensity distributions of tau along MTs segmented into two distinct populations (dim and bright) providing a quantitative signature of the condensation process (Supplementary Fig. 1c). Increasing the tau concentration progressively occluded our ability to distinguish condensates from their surroundings as overall total fluorescence increased on the MT (Fig. 1e-f). We also observed a concentration-

dependent increase in frequency, percent total coverage of the MT lattice, and size of the condensates (Fig. 1f, Supplementary Fig. 1d). Accounting for the increase in diffuse tau signal surrounding the condensate, we observed a concentration-independent density of tau within condensates, suggesting the tau molecules occupy the total available MT surface within condensate boundaries (Fig. 1g). Finally, condensates slowly dissolved after removal of soluble tau from solution (Fig. 1b, Supplementary Fig. 1b), revealing tau condensation is reversible.

Similar to observations in live cells[19], we observed that tau invariably accumulated at regions of high MT curvature (Fig. 1h), revealing that the molecule intrinsically recognizes tubulin lattice conformations. While tau bound diffusely to MTs assembled with either taxol or the non-hydrolyzable GTP analogue guanosine-5'-[(α,β)-methyleno]triphosphate (GMP-CPP), condensates only formed on taxol-stabilized, or native GDP MT lattices (Figs. 1i-j, Supplementary Fig. 1c), revealing that condensation is gated by the nucleotide state of the MT lattice. This observation likely explains the previously reported ~7-fold difference in tau's binding affinity for GMP-CPP versus GDP MTs[20]. High-resolution cryo-EM structures of GMP-CPP versus GDP MTs revealed an expansion of ~2.2 Å in the inter-tubulin dimer distance of GMP-CPP MTs[21]. We thus hypothesize that the spacing between tubulin dimers regulates tau's ability to undergo condensation on the lattice.

Tubulin's unstructured C-terminal tails have been reported to affect tau binding to MTs[10]. In these experiments, tau was labeled on its two endogenous cysteines, which have recently been suggested to make direct contact with tubulin[22], possibly confounding interpretation of this data. In our assays, removal of tubulin's tail domains by subtilisin digestion led to uniform tau binding to the digested MTs, in contrast to undigested MTs which showed clear tau condensation (Fig. 1k, Supplementary Fig. 1c). Thus, tubulin tails are required for tau condensation. Surprisingly, intensity analysis revealed that more tau bound to subtilisin digested versus WT MTs, in apparent contrast to previous results[10,23]. However, raising the total tau concentration forty-fold revealed that tau intensity was now greater on undigested MTs (Fig. 1k, Supplementary Fig. 1c). At this concentration, tau condensates are not easily discernible on WT MTs due to high amounts of total tau on the lattice. We propose that tubulin tails hinder the ability of single tau molecules to directly contact the surface of the tubulin dimer[22], but tau condensation, mediated in part by tubulin tails, facilitates direct contact with the tubulin dimer surface, resulting in a higher overall tau density on the MT lattice.

We hypothesized that tau self-association underlies condensation, and set out to test this idea. Fluorescence recovery after photobleaching (FRAP) experiments revealed that tau condensates recovered approximately two-fold more slowly than diffusely bound tau outside of condensate boundaries (Figs. 2a-b), demonstrating that bulk turnover of tau molecules is slower within condensates. We directly observed single SNAP-TMR-labeled tau molecules (Supplementary Fig. 1e) as they encountered tau condensates composed of GFP-labeled tau (Fig. 2c, Supplementary Video 2). Outside of condensates, most SNAP-TMR tau molecules rapidly diffused along the MT lattice with an average dwell time of 6.2 s (Figs. 2c-d). Single tau molecules diffused to condensate boundaries upon which their behavior altered dramatically, transitioning from highly mobile to statically bound (Fig. 2c). Consistently, the

measured diffusion coefficient was substantially reduced within condensates, from 4.6×10^{-2} um^2/sec. outside of condensate boundaries (N = 191 molecules), to 4×10^{-4} um^2/sec. within condensates (N = 108 molecules). Therefore, tau condensation dramatically reduces the molecular dynamics of tau molecules on the MT surface. Within condensates, dwell times for single tau molecules increased six-fold, indicating cooperative interactions between tau molecules underlie condensate cohesiveness (Fig. 2c-d). In further support of the dynamic nature of tau condensates (Fig. 1b-c), we observed single tau molecules transition into and out of the condensate boundary, switching behavior repeatedly between immobility and rapid diffusion (Fig. 2c). We conclude that interactions between tau molecules, gated by the MT lattice (Fig. 1), strongly reduce tau's molecular dynamics on the MT surface, providing a possible molecular mechanism for tau condensation.

Tau condensates share qualities of reversible LLPS previously observed for tau in solution[6,7,24]. Both processes are reversible, concentration dependent, result in distinct phases composed of low and high concentrations of tau, and are relatively insensitive to ionic strength [24,25]. In addition, condensates merge as they encounter one another, similar to phase-separated droplets of tau after LLPS. To explore if tau condensates share similar material properties to phase-separated tau, we exposed condensates to 1,6-hexanediol (1,6-HD), an aliphatic alcohol that is hypothesized to disrupt weak-hydrophobic interactions between proteins, and has been shown to dissolve tau LLPS droplets[24]. Tau condensates were rapidly dissolved by 1,6-HD, without affecting the overall diffuse tau binding to either taxol or GMP-CPP MTs (Fig. 2e). Therefore, phase-separated tau and MT-bound tau condensates share a similar sensitivity to 1,6-HD, and we speculate that weak hydrophobic interactions underlie both processes. However, unlike phase-separated tau in solution, tau condensates on MTs did not rapidly harden into gel-like structures[24], remaining susceptible to rapid 1,6-HD dissolution even after five hours of incubation on MTs.

We used 1,6-HD to further probe the role of the MT lattice in tau condensation. Surprisingly, tau condensates formed, dissolved upon addition of 1,6-HD, and re-formed upon 1,6-HD removal largely at the same locations on the MT lattice (Fig. 2f). We infrequently observed the formation of a new condensate, or the lack of condensate reformation after 1,6-HD removal (Fig. 2f, Supplementary Video 3). This observation indicates that local regions of the MT lattice could act as nucleation 'hot-spots' for tau condensation, though we cannot rule out that a small nucleus of tau oligomer could remain bound to these regions during 1,6-HD exposure. However, tau condensation was sporadic at certain hot-spots, suggesting that a lingering tau nucleus is not strictly required for condensation (Fig. 2f). These hot-spots may represent areas of local lattice distortion, similar to the highly curved regions that invariably accumulate tau (Fig. 1h). Our results show that tau condensation is reversible, and likely driven by the same types of molecular interactions between tau molecules that lead to LLPS of tau in solution. The slower kinetics of FRAP recovery, and longer dwell-times within condensates differ from the typical properties of an LLPS system in solution[24], which we surmise may be due to scaffolded interactions of tau molecules with the MT.

We next sought evidence that tau condensation can occur *in vivo*. We stained mouse hippocampal neurons with two different pan-tau antibodies at various days after plating, and observed developmentally dependent tau localization to puncta along MTs, which strikingly

resembled tau condensates *in vitro* (Figs. 2g, Supplementary Fig. 2). These puncta were not as apparent in DIV3 or DIV4 neurons, even after axon specification marked by dephospho-specific tau-1 antibody staining (Supplementary Fig. 2a). However, by DIV7, tau puncta were abundant in all neurons (Supplementary Fig. 2). Similar staining has been reported[26-28], and some suggest that because tau puncta are resistant to Triton X-100 extraction, they represent tau aggregates. However, in vitro, tau condensates were similarly resistant to Triton X-100 (Fig. 2h), raising questions about this interpretation. Overexpression of tau results in regions of higher tau density along neurite processes[29], which may be similar to the tau foci observed here. Thus, tau localization in neurons is diverse, and puncta of tau resembling tau condensates form inside of neurons in a developmentally regulated manner.

Next, we set out to map the regions of tau responsible for self-association within condensates. In neurons, six tau isoforms exist, differing in the number of projection domain inserts (N) and of MT binding repeats (R). All isoforms contain a microtubule-binding domain (MTBD) flanked by a proline-rich region and pseudo-repeat region (Fig. 3a). Alternative splicing in the MTBD or projection domain did not grossly perturb tau condensation (Fig. 3a-b, Supplementary Fig. 1a). We assayed for tau oligomerization by first forming condensates with full-length mScarlet-tagged tau (2N4R), followed by introduction of equimolar amounts of various GFP-tagged tau isoforms (2N4R/2N3R/0N3R). We compared the enrichment of GFP-tau isoform signal within the boundaries of full-length mScarlet-tau condensates, versus GFP signal outside of mScarlet-tau condensates. We observed a two- to three-fold enrichment of GFP-2N4R, −2N3R, and −0N3R isoforms within mScarlet-tau condensates, indicating that alternative splicing does not grossly affect the ability of a tau molecule to incorporate into 2N4R tau condensates (Fig. 3c, Supplementary Fig. 3).

We truncated different domains of tau and found that, in contrast to published data on tau LLPS[7], the MTBD alone was weakly excluded from condensates, while the isolated projection domain exhibited only diffuse binding (Figs. 3a, c, Supplementary Figs. 1a, 3c). The isolated C-terminus of tau segregated into condensates, though more weakly than full-length tau (1.2-fold vs. 2.9-fold), as did a “bonsai” construct consisting of a fusion between the N- and C-terminus, but lacking the MTBD (1.3-fold, Figs. 3a, 3c, Supplementary Fig. 3c). These data indicate that the C-terminus of tau licenses other portions of the molecule into condensates. Consistently, while the MTBD was excluded from condensates, the addition of the flanking N-terminal proline-rich and C-terminal pseudo-repeat domains (mini-tau) restored segregation into condensates to near full-length tau levels (Figs. 3a, c, Supplementary Fig. 3d). The C-terminal pseudo-repeat domain is evolutionarily conserved and contains several aliphatic residues (Supplementary Fig. 3e). Truncation of residues from the pseudo-repeat region of mini-tau resulted in a progressive decrease in condensate incorporation, indicating that tau condensation requires interactions via multiple amino acids located within this region (Fig. 3d, Supplementary Fig. 3d). Removal of the entire pseudo-repeat domain (mini-tauΔ28) largely abolished incorporation into 2N4R tau condensates (Fig. 3d, Supplementary Fig. 3d). Our data suggest that potential hydrophobic interactions within the pseudo-repeat region are important for the intermolecular interactions that underlie tau condensation. Interestingly, this region was previously shown to enhance tau’s

MT affinity, and disease-associated mutations within this domain affect the dynamicity of tau on MTs in living cells[30].

Previous studies have suggested that tau can regulate the movement of molecular motors, including the cytoplasmic dynein-dynactin complex[9,14]. However, this reported dynein-dynactin behavior[9] is not broadly consistent with the strongly processive movement of activated dynein-dynactin-cargo adapter complexes discovered subsequently[31]. To reconcile these findings, we investigated the effects of tau condensates on the motility of activated dynein-dynactin-cargo adapter complexes. We found the majority of processive dynein-dynactin-BicD2N (DDB)[31] complexes passed through condensates (84%), often displaying dramatic pausing at the condensate boundary (49%) (Fig. 4a, Supplementary Fig. 4a-b, Supplementary Video 4). A small population of motor complexes (~3%) exhibited unidirectional movement before switching to a bidirectional state at tau condensates (Supplementary Fig. 4b-c). Similarly, DDB motors that displayed only diffusive behavior on the MT[31] reversed direction at tau condensates, (Fig. 4b, Supplementary Fig. 4b). This behavior was very similar to a purified p150^{glued} construct, a component of the dynactin complex, which diffuses along MTs via interactions with the tubulin tail domains[32] (Fig. 4b). We conclude that tau condensates are permissive to processive dynein movement, but not to dynactin-mediated diffusion. Thus, in contrast to the plus-end directed motor kinesin-1[9,13,25,33], dynein is physically capable of traversing tau condensates. The behavioral difference between these motors can be explained by recent cryo-EM structures of tau on the MT[22]. While the kinesin motor domain has a large steric clash with MT-bound tau, we found that the much smaller dynein MT binding domain does not (Fig. 4c, Supplementary Fig. 4d-f). Combined with recent work showing how orthogonal MAP proteins facilitate kinesin-1 transport[12], our results provide a comprehensive view for how tau may directly modulate the bidirectional movement of intracellular cargos driven by dynein and kinesin-1.

We sought to determine the domains of tau that contribute to the dramatic pausing of processive dynein complexes (Fig. 4a). Condensates formed from the shortest natural tau isoform (0N3R) or the mini-tau construct, allowed progressively greater numbers of motor complexes to pass unimpeded (47% and 63%, respectively) (Fig. 4d, Supplementary Fig. 4b). Further, we found that motor behavior was not correlated with peak pixel intensity within tau condensates (Fig. 4e), indicating that the distribution of motor behaviors does not depend on any differences of tau density within condensates.

Recent data have defined adaptor-dependent variations in the number of dynein dimers linked to the dynactin scaffold[34]. BicD2N predominantly recruits only one dynein dimer, while the adapter Hook3 largely recruits two dynein dimers per dynactin. Dynein-dynactin-Hook3 (DDH) complexes passed through tau condensates without pausing at significantly higher rates (55%) compared to DDB (35%), indicating that pairs of dynein dimers are better able to navigate tau condensates unimpeded (Figs. 4f, Supplementary Fig. 4b). Dynein-dynactin-Rab11-FIP3 (DDF), exhibited significantly increased rates of passing through tau condensates without pausing (68%), indicating that Rab11-FIP3, likely recruits a pair of dynein dimers similar to Hook3 (Fig. 4f Supplementary Fig. 4b). Another dynein regulator, LIS1, directly impinges on dynein's mechanochemistry, and allosterically controls

DDB velocity[35,36]. Analysis of DDB complexes that contained bound Lis1 (DDB-L) revealed that these complexes were also significantly better at crossing tau condensates unimpeded (59% vs. 35%) (Fig. 4g, Supplementary Fig. 4b). These results reveal that allosteric control of dynein motor activity alters the motor's ability to traverse condensates, and suggest that tau condensation could modulate the velocity and run-lengths of retrograde traffic in a cargo-dependent manner in vivo. In this context, we note that changes in dynein run-lengths result in neurodegenerative and neurodevelopmental phenotypes[37,38]

The molecular mechanism for tau-mediated inhibition of MT severing is unknown. We found that a truncated, active form of the MT severing enzyme spastin[39] was largely excluded from tau condensates (Fig. 4h). As a result, tau condensates protected the underlying MT lattice from spastin-mediated severing, while the lattice surrounding the condensate was destroyed (Fig. 4h, Supplementary Video 5). Complementary results presented in this issue[25] reveal that this principle extends to the other major MT severing enzyme, katanin. Consequently, tau condensates affect both molecular motor movement and MT severing by acting as selectively permissible barriers for MT effector proteins.

Phosphorylation plays a key role in tau biology and disease. The recombinant tau protein used in this study was produced in bacteria and therefore contains no post-translational phosphorylation. We observe only minor differences in MT-binding affinity and condensation kinetics between our study and that of Siahaan et al.[25], which utilized baculovirus-expressed, partially phosphorylated tau[40]. Therefore tau phosphorylation is not required for condensation, but may tune the kinetics of condensate formation and growth via modulation of tau's affinity for the MT, and potentially the tau interactions that drive condensation.

In summary, our study has uncovered a regulated form of reversible tau oligomerization that functionally compartmentalizes the MT lattice. We propose that tau condensation is a physiological form of tau self-association, gated and scaffolded by the MT lattice, which can be harnessed by cells to spatially direct diverse MT-based molecular pathways. Further, our results demonstrate that oligomerization is not exclusive to the pathological form of tau. Because tau condensation is sensitive to total tau concentration, we speculate that loss of tau monomer to alternative self-association pathways, such as the fibrillization observed in tauopathies, will negatively impact tau condensate formation, dynamics, and functions in neurons.

Methods

Microtubule Assembly

Porcine brain tubulin was isolated using the high-molarity PIPES procedure as described and then labeled with biotin-, Dylight-405 NHS-ester, or Alexa647 NHS-ester as described (http://mitchison.hms.harvard.edu/files/mitchisonlab/files/labeling_tubulin_and_quantifying_labeling_stoichiometry.pdf). Pig brains were obtained from a local slaughterhouse and used within ~4 hours after death. Microtubules were prepared by incubation of 100 uM tubulin with 1mM GTP for 10 min. at 37°C, followed by dilution into 20 μM final taxol for an additional 20 min. GMP-CPP MTs were prepared

similarly but with 1mM GMP-CPP instead of GTP without taxol. Microtubules were pelleted at 80K rpm over a 25% sucrose cushion in a TLA-100 rotor and the pellet was resuspended in 50 μL BRB80 containing 10 μM taxol. For removal of tubulin C-terminal tails, microtubules were further treated with subtilisin for 1 hour at 37 degrees as described *(23)*. The reaction was terminated by 1 mM PMSF and pelleted at 80K rpm as before. Concentration of subtilisin used and digestion were assayed by Coomassie staining and recombinant $p150^{glued}$ binding. For GMP-CPP capped microtubules, 20 μM of Alexa647-labelled and biotin-labelled tubulin was added to 0.5 mM GMPCPP in BRB80 (80 mM potassium PIPES, pH 6.8, 1mM MgCl2, 1 mM EGTA) at 37°C for half an hour. Then 10 mM GTP was added along with 40 μM Alexa405-labelled tubulin for an additional half an hour. Finally, 20uM Alexa647-labelled and biotin-labeled tubulin was added along with 1 mM GMPCPP for at least half an hour. Capped MTs were kept at 37°C until use. In GMP-CPP capped microtubule experiments, N is defined as the number of preparations of microtubules used to derive images.

Protein Constructs

All human tau and spastin constructs were cloned into pET28A vector using Gibson assembly. Constructs contain a N-terminal cassette consisting of: a 6x His-tag and tandem Strep-tags connected by a GS-linker. The sequence is as follows: MGSSHHHHHHSSGLVPRGSHMWSHPQFEKGGGSGGGSGGSAWSHPQFEKGS. This cassette is then followed by the fluorophore (sfGFP/mScarlet/SNAPf) followed by a precision protease cleavage site. Human spastin cDNA was purchased from Transomics (BC150260). A fully active, truncated spastin (Δ227) was cloned into pET28-strepII-sfGFP. Full-Length human tau was purchased from Addgene (#16316). Amino acid boundaries for tau constructs are as described in Fig. 3A. In short, the projection domain inserts were from E45-T102. The Proline-rich domain encompassed S198-L243, and the MTBD was defined as Q244-E372. The second repeat (exon 10) removed in 3R tau constructs spans K274-G304. The pseudo repeat region consists of T373-V399.

Protein Purification

Tau and Spastin were expressed in BL21(DE3) cells (Agilent). The cells were grown at 36° C until OD_{600} of 0.6, then induced with 0.4 mM IPTG overnight at 18 ° C. Cells were resuspended in buffer X and lysed using an Emulsiflex C-3 (Avestin). Proteins were affinity-purified on Strep XT beads (IBA). Tau constructs were further purified by anion exchange on a HiTrap Q HP column in Protein Buffer pH 7.5 (50 mM Tris-HCl pH 7.5, 2 mM $MgCl_2$, 1mM EGTA, and 10% glycerol) with a salt gradient from 100 mM to 400 mM. Full-length tau constructs were further purified by size exclusion chromatography on a Superose 6 10/300 column in Protein Buffer pH 8. All Mini-Tau based constructs were induced for only 4 hours and were purified similarly to all other tau construct. For Mini-Tau constructs and Spastin, we performed cation exchange on a HiTrap SP HP column with the same conditions as other tau constructs. Dynein-Dynactin-Cargo Adaptor complexes were purified from rat brain lysate as described[31]. Briefly, all SNAPf-tagged adapter protein constructs were purified by Strep-tag affinity as above and further purified by size exclusion chromatography on a Superose 6 10/300 column in 60 mM Hepes pH 7.4, 50 mM K-acetate, 2 mM $MgCl_2$, 1 mM EGTA, 10 % glycerol. Dynein-Dynactin-adapter complexes were labeled with in a ~4:1

ratio of dye:SNAPf-tagged protein at 2 μM SNAP-TMR, SNAP-Alexa647, or SNAP-Alexa488 dye (NEB) during the isolation procedure and were frozen in small aliquots and stored at −80°C. The protein concentration was assessed using a Nanodrop One (ThermoFisher). Protein concentrations given are for the total amount of fluorophore (monomer) in the assay chamber. All buffers and chemicals were from Sigma Aldrich.

TIRF Microscopy

All TIRF microscopy was performed on a custom built through the objective TIRF microscope (Technical Instruments, Burlingame CA) based on a Nikon Ti-E stand, motorized ASI stage, quad-band filter cube (Chroma), Andor laser launch (100 mW 405 nm, 150 mW 488 nm, 100 mW 560 nm, 100 mW 642 nm), EMCCD camera (iXon Ultra 897), and high-speed filter wheel (Finger Lakes Instruments). All imaging was performed using a 100X 1.45NA objective (Nikon) and the 1.5X tube lens setting on the Ti-E. Experiments were conducted at room temperature. The microscope was controlled with Micro-manager software. For imaging Tau binding at 20 nM (Fig. 1K), an 8X neutral density filter was used to reduce total signal intensity.

TIRF chambers were assembled from acid washed coverslips (http://labs.bio.unc.edu/Salmon/protocolscoverslippreps.html) and double-sided sticky tape. Taxol-stabilized MTs were assembled with incorporation of ~ 10% Dylight-405- or Alexa647-, and biotin-labeled tubulin. Chambers were first incubated with 0.5 mg/mL PLL-PEG-Biotin (Surface Solutions Inc.) for 10 min., followed by 0.5 mg/mL streptavidin for 5 min. Microtubules were diluted into BC Buffer (80mM Pipes pH 6.8, 1mM $MgCl_2$, 1mM EGTA, 1 mg/mL BSA, 1mg/mL casein, 10μM taxol) then incubated in the chamber and allowed to adhere to the streptavidin-coated surface for 10 minutes. Unbound MTs were washed away with TIRF buffer (60 mM Hepes pH 7.4, 50 mM K-acetate, 2 mM $MgCl_2$, 1 mM EGTA, 10 % glycerol, 0.5 % Pluronic F-127, 0.1 mg/mL Biotin-BSA, 0.2 mg/mL κ-casein, 10μM taxol). Unless otherwise stated, experiments were conducted in imaging buffer (60 mM Hepes pH 7.4, 50 mM K-acetate, 2 mM $MgCl_2$, 1 mM EGTA, 10 % glycerol, 0.5 % Pluronic F-127, 0.1 mg/mL Biotin-BSA, 0.2 mg/mL κ-casein, 10μM taxol, 2 mM Trolox, 2 mM protocatechuic acid, ~50 nM protocatechuate-3,4-dioxygenase, and 2 mM ATP). Unless specifically stated, all tau assays were performed with 0.5 nM tau and incubated for at least 5 minutes before imaging.

The resulting data was analyzed manually in ImageJ (FIJI). For images displayed in figures, background was subtracted in FIJI using the ‘subtract background’ function with a rolling ball radius of 50 and brightness and contrast settings were modified linearly. In images where there was substantial drift, the “Descriptor-based series registration (2D/3D + T)” plug-in was used in FIJI with interactive brightness and size detections in the MT channel to register the images.

Continuous imaging assays

Tau condensation assays (Figa. 1a-c, Supplementary Fig. 1b) were conducted in Cellvis 96-well Glass Bottom Plate (Cellvis, #P96–1.5H-N). For washout experiments double-sided sticky tape chambers were assembled with 22 × 40 mm coverglass perpendicular to the glass slide. The coverslip was then sealed to the coverglass by epoxy. The extra coverglass area

allowed for seamless buffer exchange during imaging. For wash-in, and 1,6-hexanediole experiments, images were taken one second apart until the end of the assay. For wash-out assays, images were taken every 30 seconds. Intensity was measured manually using kymographs on ImageJ. Time zero was defined as the point of visible condensate nucleation. N is defined as the number of chambers imaged in the dataset.

Photobleaching Experiments

FRAP experiments: Images were acquired on a TIRF microscope built by Nikon using a Nikon Ti2 stand, LU-n4 four laser unit, EMCCD camera (iXon Ultra 897), and high-speed filter wheel (Finger Lakes Instruments). Stimulation was directed using a miniscanner coupled with a motorized Ti2-LAPP system and powered by a 405nm laser (100mW) using a 405nm Reflect/430–800nm Transmit Mirror for L-APP Dual TIRF. All imaging was performed using a 100X 1.45NA objective (Nikon) and the 1.5X tube lens setting on the Ti2. All experiments were done at 25°C. For the FRAP experiments a pre-bleach image was acquired by averaging 8–10 consecutive images. Then 8 regions were bleached (2 background, 4 condensate, 4 lattice) at 2% power without scanning. 5 images were taken before stimulation and 150 images were taken after stimulation all at 1 second intervals.

Plots were generated using NIS-Elements AR software and exported to excel. The background subtracted average intensity was measured in a region of interest (ROI) overtime and normalized to the initial fluorescence intensity within the first 5 frames. Data from 24 condensate and lattice regions were analyzed and pooled from experiments from two days with two different protein preparations. In figure legends, N is defined as number of chambers used.

Single molecule diffusion measurements

Tracks of molecules were assessed for co-localization with condensates by manual inspection. On rare occasions, tracks were found to briefly co-localize with the condensates but were mostly motile outside such regions. These latter tracks were not considered for analysis of diffusion within the condensates. A total of 108 tracks were thus identified and their MSD curves were then calculated and averaged. The diffusion coefficient which was estimated from the averaged curve was computed ($<x^2>=2Dt$) found to be 3.94e-4 micron^2/sec.

Of note, some tau molecules were found to localize outside of MTs. Tracks from such molecules tended to show diffusion coefficient of order 1e-4. This can be taken as an estimate of background drift and vibration of the optical stage and is sufficiently low that it can be hard to computationally correct. Crucially, any such drift is lower than the diffusion within condensates. Therefore 3.94e-4 micron^2/sec. may be a slight overestimate but not a major departure from the true value.

Single molecule spiking experiments

2N4R SNAPf-Tau was labeled with TMR dye in a 1:4 molar ratio for 2 hours before size exclusion with Zeba Spin Desalting Column (Thermo Scientific #89882). Then, 0.5 nM GFP-Tau was flowed in to first form condensates. Next, a mixture of 0.5 nM GFP-Tau and

10–25 pM TMR-Tau was flowed in the chamber. Images in the TMR channel were taken every 0.25 seconds. Images were taken every second to measure single molecule dwell times. We used the GFP channel as a fiducial for dwell times inside and outside of condensates. Only molecules whose entire residency on the MT lattice was captured, inside or outside condensates, were counted. N is defined as the number of chambers used.

Primary Neuronal Cultures and Analysis.

Cultured neurons were obtained from embryonic day 16.5 (E16.5) mouse embryonic hippocampi. Hippocampi were carefully dissected and meninges removed. Dissociation was achieved by a combination of enzymatic digestion using papain and pipetting homogenization (Worthington Biochemical Corporation). Neurons were resuspended in neuron growth media (Neurobasal media containing 2% B27 supplement, 2% GlutaMAX solution, glucose, and penicillin/streptomycin). A total of ~10^5 neurons were plated in poly-D-Lysine-coated coverslips. Growth media was changed every two days. The morning a vaginal plug was observed was considered E0.5. All animals were used with approval from the University of California Davis Institutional Animal Care and Use Committees. The use of animals complied with all relevant ethical regulations regarding animal research.

At the desired day in vitro (DIV), the neurons were fixed in 4% PFA for 20 minutes and permeabilized with 0.3% Triton-X for 5 minutes. Neurons were blocked with 5% BSA and incubated with primary antibody at a 1:500 dilution (Tau – Genetex #49353, or Thermo Scientific #13–6400, Beta-Tubulin – Abcam #ab6046), followed fluorescently-labelled secondary antibody at a 1:1000 dilution (Anti-chicken – A11039, Anti-mouse – A28175, A28180, Anti-rabbit - A27039), and mounted with Vectashield.

Coverslips were imaged on a Leica TCS SPE-II RYBV with automated DMi8 with a Leica laser launch (25 mW 405 nm, 10 mW 488 nm, 20 mW 561 nm, 18 mW 635 nm). All imaging was performed using a HC PL APO CS2 63X 1.40NA objective (Leica) Experiments were conducted at room temperature. The microscope was controlled with Leica LAS X software and analyzed with ImageJ. For qualitative images, N is defined as the number of neuronal preparations used.

For quantification of tau puncta, the brightest plane for a given z stack was selected for analysis. The non-neuronal was filtered via its low intensity, although bright spots outside of neuronal area were also occasionally masked out by hand. The loci of tau enhancement in all cases were identified by fitting local intensity to Gaussian or quadratic profile. Good fits were identified via imposing a limit on squared residuals and cutoffs on fitted peak widths in x and y (both to avoid fitting single pixel specs and large broad peaks such as cell bodies). All cutoffs were held the same for all data being analyzed. The density of enhanced tau loci was quantified as the number of loci divided by the number of pixels corresponding to neuronal fluorescence.

Data Analysis for Condensate Enrichment (Fig. 3)

mScarlet-tagged 2N4R tau condensates were used as fiducials for condensate boundaries. Background subtracted mean intensities were obtained for a linescan along the microtubule. Each straight and uninterrupted (no MT overlaps) stretch of MT was counted as a single data

point. Data points from two different protein preparations of mScarlet-labeled 2N4R tau condensates were pooled. Fold enrichment was calculated by dividing each data point for condensate intensity by the average value of associated lattice intensity.

Dynein-Dynactin-Adapter Behavior Assays

DDX movement was visualized manually using kymographs. The behaviors at condensates were characterized in the following manner. A loss of signal at a condensate was binned as “detach”. Continuing through the condensate boundary without a change in velocity was binned as “pass”. A “pause” was defined as a diffraction limited stop in processivity for longer than 3 frames (1.5 sec.). These molecules were then binned as pause-pass and pause-detach following the same behaviors as above. “Bidirectional” was binned as molecules that exhibit diffraction limited movement towards a single direction for longer than 1 micron, then reversed direction upon encountering a condensate.

Peak tau intensity for a condensate was derived by first averaging the intensities per pixel over time for a condensate throughout the entire movie. In the event of significant stage drift, the intensities at the time of the events were used. The “Find Peaks” plug-in using default conditions for ImageJ was then used to determine the peak intensity. Background intensity of a non-MT region nearby was then subtracted from this value to determine background subtracted peak intensity.

Single Molecule Intensity and Photobleaching Analysis

The FIJI plugin ComDet was used to analyze the intensities of TMR-labeled SNAP-2N4R-tau molecules bound to MTs. The estimated particle size was set to three pixels and the intensity threshold was set to three SD. Photobleaching analysis was carried out on TMR-labeled SNAP-2N4R-tau molecules that were non-specifically bound to the observation chamber to avoid the confounding factors of tau diffusion and dissociation from MTs. Kymographs were generated by drawing a line across these molecules and the intensity of the molecules was then plotted against time. Photobleaching steps were then assessed manually by visual inspection of the intensity plots.

Quantification of Spastin Severing

Linear regions of MT lattice inside and outside condensates were identified, and the MT intensity at the end of acquisition (~10 minutes) was normalized to initial MT intensity from the first frame. MT regions that detached from the coverslip during the severing reaction were excluded from analysis.

Intensity Distribution Analysis

Pixel intensities were obtained from continuous uninterrupted regions along the MT as in Fig.3. The pixel intensities were normalized to the average pixel intensity of all regions in the same field of view to normalize for changes in imaging conditions (laser intensity, TIRF angle, etc.). All normalized values were aggregated and graphed on a relative frequency plot.

Statistics and Reproducibility

All data was collected from at least two independent trials with at least three independent experimental chambers per trial. All repeated independent experiments showed similar results. Unless otherwise stated, all data was analyzed manually using ImageJ (FIJI). Graphs were created using Graphpad Prism 7.0a and 8.0.1, and statistical tests were performed using this program. Major points on graphs represent data means with error bars representing variation or associated estimates of uncertainty. For comparison of DDB behaviors at condensates, the data was collected into a contingency table with four assay conditions and five observable outcomes.

For data in Fig. S4B, the aggregate analysis of the observed outcome frequencies for the entire table was performed using the Pearson's chi-squared test and showed significance at very high levels ($p < 0.0001$). However, some outcome counts were low (below 5) so the analysis was redone using Fisher's exact test and again significance was extremely high ($p < 0.0001$). DDB outcomes were compared pairwise with other assay conditions (using data for all outcomes and for just "Pass"/"Pause Pass" pair of outcomes) and significant differences ($p < 0.0001$) were seen for all comparisons using both tests. Where appropriate, statistical tests were two-sided.

Data Availability

Source data for all statistical analyses can been found on Supplementary Table 1. All other data that support the findings of this study are available from the corresponding authors upon reasonable request.

Code Availability

The custom analysis code used in this study is available from the corresponding authors upon reasonable request.

Supplementary Material

Refer to Web version on PubMed Central for supplementary material.

Acknowledgments

We would like to thank all the members of the McKenney and Ori-McKenney labs for critical feedback and Brigette Monroy for initial tau observations. We thank Jawdat Al-Bassam for feedback and Marcus Braun, and Stefan Diez the sharing of unpublished data. We apologize to the authors of many excellent studies that we failed to cite due to space constraints.

Funding

R.J.M is supported by grants R00NS089428 from NINDS and R35GM124889 from NIGMS. K.M.O.-M. is supported by grants R00HD080981 from NICHD, and A19–0406 from the Pew Charitable Trusts. S.S. is supported by grant R01NS109176. MV is supported by grant NSF ENG-1563280.

References

1. Goedert M, Eisenberg DS & Crowther RA Propagation of Tau Aggregates and Neurodegeneration. Annu Rev Neurosci 40, 189–210, doi:10.1146/annurev-neuro-072116-031153 (2017). [PubMed: 28772101]

2. Kapitein LC & Hoogenraad CC Building the Neuronal Microtubule Cytoskeleton. Neuron 87, 492–506, doi:10.1016/j.neuron.2015.05.046 (2015). [PubMed: 26247859]

3. Li XH & Rhoades E Heterogeneous Tau-Tubulin Complexes Accelerate Microtubule Polymerization. Biophys J 112, 2567–2574, doi:10.1016/j.bpj.2017.05.006 (2017). [PubMed: 28636913]

4. Makrides V et al. Microtubule-dependent oligomerization of tau. Implications for physiological tau function and tauopathies. J Biol Chem 278, 33298–33304, doi:10.1074/jbc.M305207200 (2003). [PubMed: 12805366]

5. Wegmann S, Bennett RE, Amaral AS & Hyman BT Studying tau protein propagation and pathology in the mouse brain using adeno-associated viruses. Methods Cell Biol 141, 307–322, doi:10.1016/bs.mcb.2017.06.014 (2017). [PubMed: 28882310]

6. Hernandez-Vega A et al. Local Nucleation of Microtubule Bundles through Tubulin Concentration into a Condensed Tau Phase. Cell reports 20, 2304–2312, doi:10.1016/j.celrep.2017.08.042 (2017). [PubMed: 28877466]

7. Ambadipudi S, Biernat J, Riedel D, Mandelkow E & Zweckstetter M Liquid-liquid phase separation of the microtubule-binding repeats of the Alzheimer-related protein Tau. Nature communications 8, 275, doi:10.1038/s41467-017-00480-0 (2017).

8. McVicker DP, Hoeprich GJ, Thompson AR & Berger CL Tau interconverts between diffusive and stable populations on the microtubule surface in an isoform and lattice specific manner. Cytoskeleton 71, 184–194, doi:10.1002/cm.21163 (2014). [PubMed: 24520046]

9. Dixit R, Ross JL, Goldman YE & Holzbaur EL Differential regulation of dynein and kinesin motor proteins by tau. Science 319, 1086–1089 (2008). [PubMed: 18202255]

10. Hinrichs MH et al. Tau protein diffuses along the microtubule lattice. J Biol Chem 287, 38559–38568, doi:10.1074/jbc.M112.369785 (2012). [PubMed: 23019339]

11. Vershinin M, Carter BC, Razafsky DS, King SJ & Gross SP Multiple-motor based transport and its regulation by Tau. Proc Natl Acad Sci U S A 104, 87–92 (2007). [PubMed: 17190808]

12. Monroy BY et al. Competition between microtubule-associated proteins directs motor transport. Nature communications 9, 1487, doi:10.1038/s41467-018-03909-2 (2018).

13. Seitz A et al. Single-molecule investigation of the interference between kinesin, tau and MAP2c. EMBO J 21, 4896–4905 (2002). [PubMed: 12234929]

14. Vershinin M, Xu J, Razafsky DS, King SJ & Gross SP Tuning microtubule-based transport through filamentous MAPs: the problem of dynein. Traffic 9, 882–892 (2008). [PubMed: 18373727]

15. Vale RD Severing of stable microtubules by a mitotically activated protein in Xenopus egg extracts. Cell 64, 827–839 (1991). [PubMed: 1671762]

16. Qiang L, Yu W, Andreadis A, Luo M & Baas PW Tau protects microtubules in the axon from severing by katanin. J Neurosci 26, 3120–3129, doi:10.1523/JNEUROSCI.5392-05.2006 (2006). [PubMed: 16554463]

17. Yu W et al. The microtubule-severing proteins spastin and katanin participate differently in the formation of axonal branches. Mol Biol Cell 19, 1485–1498, doi:10.1091/mbc.E07-09-0878 (2008). [PubMed: 18234839]

18. Zempel H & Mandelkow EM Tau missorting and spastin-induced microtubule disruption in neurodegeneration: Alzheimer Disease and Hereditary Spastic Paraplegia. Mol Neurodegener 10, 68, doi:10.1186/s13024-015-0064-1 (2015). [PubMed: 26691836]

19. Ettinger A, van Haren J, Ribeiro SA & Wittmann T Doublecortin Is Excluded from Growing Microtubule Ends and Recognizes the GDP-Microtubule Lattice. Curr Biol 26, 1549–1555, doi:10.1016/j.cub.2016.04.020 (2016). [PubMed: 27238282]

20. Duan AR et al. Interactions between Tau and Different Conformations of Tubulin: Implications for Tau Function and Mechanism. J Mol Biol 429, 1424–1438, doi:10.1016/j.jmb.2017.03.018 (2017). [PubMed: 28322917]

21. Zhang R, LaFrance B & Nogales E Separating the effects of nucleotide and EB binding on microtubule structure. Proc Natl Acad Sci U S A 115, E6191–E6200, doi:10.1073/pnas.1802637115 (2018). [PubMed: 29915050]

22. Kellogg EH et al. Near-atomic model of microtubule-tau interactions. Science 360, 1242–1246, doi:10.1126/science.aat1780 (2018). [PubMed: 29748322]

23. Hagiwara H, Yorifuji H, Sato-Yoshitake R & Hirokawa N Competition between motor molecules (kinesin and cytoplasmic dynein) and fibrous microtubule-associated proteins in binding to microtubules. J Biol Chem 269, 3581–3589 (1994). [PubMed: 8106402]
24. Wegmann S et al. Tau protein liquid-liquid phase separation can initiate tau aggregation. EMBO J 37, doi:10.15252/embj.201798049 (2018).
25. Siahaan V et al. Kinetically distinct phases of tau on microtubules regulate kinesin motors and severing enzymes. Nature Cell Biology **This Issue** (2019).
26. Kremer A et al. Early improved and late defective cognition is reflected by dendritic spines in Tau.P301L mice. J Neurosci 31, 18036–18047, doi:10.1523/JNEUROSCI.4859-11.2011 (2011). [PubMed: 22159117]
27. Garcia-Leon JA et al. Generation of a human induced pluripotent stem cell-based model for tauopathies combining three microtubule-associated protein tau mutations which displays several phenotypes linked to neurodegeneration. Alzheimers Dement, doi:10.1016/j.jalz.2018.05.007 (2018).
28. Hubbard KS et al. High yield derivation of enriched glutamatergic neurons from suspension-cultured mouse ESCs for neurotoxicology research. BMC Neurosci 13, 127, doi: 10.1186/1471-2202-13-127 (2012). [PubMed: 23095170]
29. Konzack S, Thies E, Marx A, Mandelkow EM & Mandelkow E Swimming against the tide: mobility of the microtubule-associated protein tau in neurons. J Neurosci 27, 9916–9927, doi: 10.1523/JNEUROSCI.0927-07.2007 (2007). [PubMed: 17855606]
30. Niewidok B et al. Presence of a carboxy-terminal pseudorepeat and disease-like pseudohyperphosphorylation critically influence tau's interaction with microtubules in axon-like processes. Mol Biol Cell 27, 3537–3549, doi:10.1091/mbc.E16-06-0402 (2016). [PubMed: 27582388]
31. McKenney RJ, Huynh W, Tanenbaum ME, Bhabha G & Vale RD Activation of cytoplasmic dynein motility by dynactin-cargo adapter complexes. Science 345, 337–341, doi:10.1126/science. 1254198 (2014). [PubMed: 25035494]
32. McKenney RJ, Huynh W, Vale RD & Sirajuddin M Tyrosination of alpha-tubulin controls the initiation of processive dynein-dynactin motility. EMBO J, doi:10.15252/embj.201593071 (2016).
33. McVicker DP, Chrin LR & Berger CL The nucleotide-binding state of microtubules modulates kinesin processivity and the ability of Tau to inhibit kinesin-mediated transport. J Biol Chem 286, 42873–42880, doi:10.1074/jbc.M111.292987 (2011). [PubMed: 22039058]
34. Urnavicius L et al. Cryo-EM shows how dynactin recruits two dyneins for faster movement. Nature 554, 202–206, doi:10.1038/nature25462 (2018). [PubMed: 29420470]
35. Gutierrez PA, Ackermann BE, Vershinin M & McKenney RJ Differential effects of the dynein-regulatory factor Lissencephaly-1 on processive dynein-dynactin motility. J Biol Chem, doi: 10.1074/jbc.M117.790048 (2017).
36. Baumbach J et al. Lissencephaly-1 is a context-dependent regulator of the human dynein complex. Elife 6, doi:10.7554/eLife.21768 (2017).
37. Ori-McKenney KM, Xu J, Gross SP & Vallee RB A cytoplasmic dynein tail mutation impairs motor processivity. Nat Cell Biol 12, 1228–1234, doi:10.1038/ncb2127 (2010). [PubMed: 21102439]
38. Hoang HT, Schlager MA, Carter AP & Bullock SL DYNC1H1 mutations associated with neurological diseases compromise processivity of dynein-dynactin-cargo adaptor complexes. Proc Natl Acad Sci U S A 114, E1597–E1606, doi:10.1073/pnas.1620141114 (2017). [PubMed: 28196890]
39. White SR, Evans KJ, Lary J, Cole JL & Lauring B Recognition of C-terminal amino acids in tubulin by pore loops in Spastin is important for microtubule severing. J Cell Biol 176, 995–1005, doi:10.1083/jcb.200610072 (2007). [PubMed: 17389232]
40. Tepper K et al. Oligomer formation of tau protein hyperphosphorylated in cells. J Biol Chem 289, 34389–34407, doi:10.1074/jbc.M114.611368 (2014). [PubMed: 25339173]

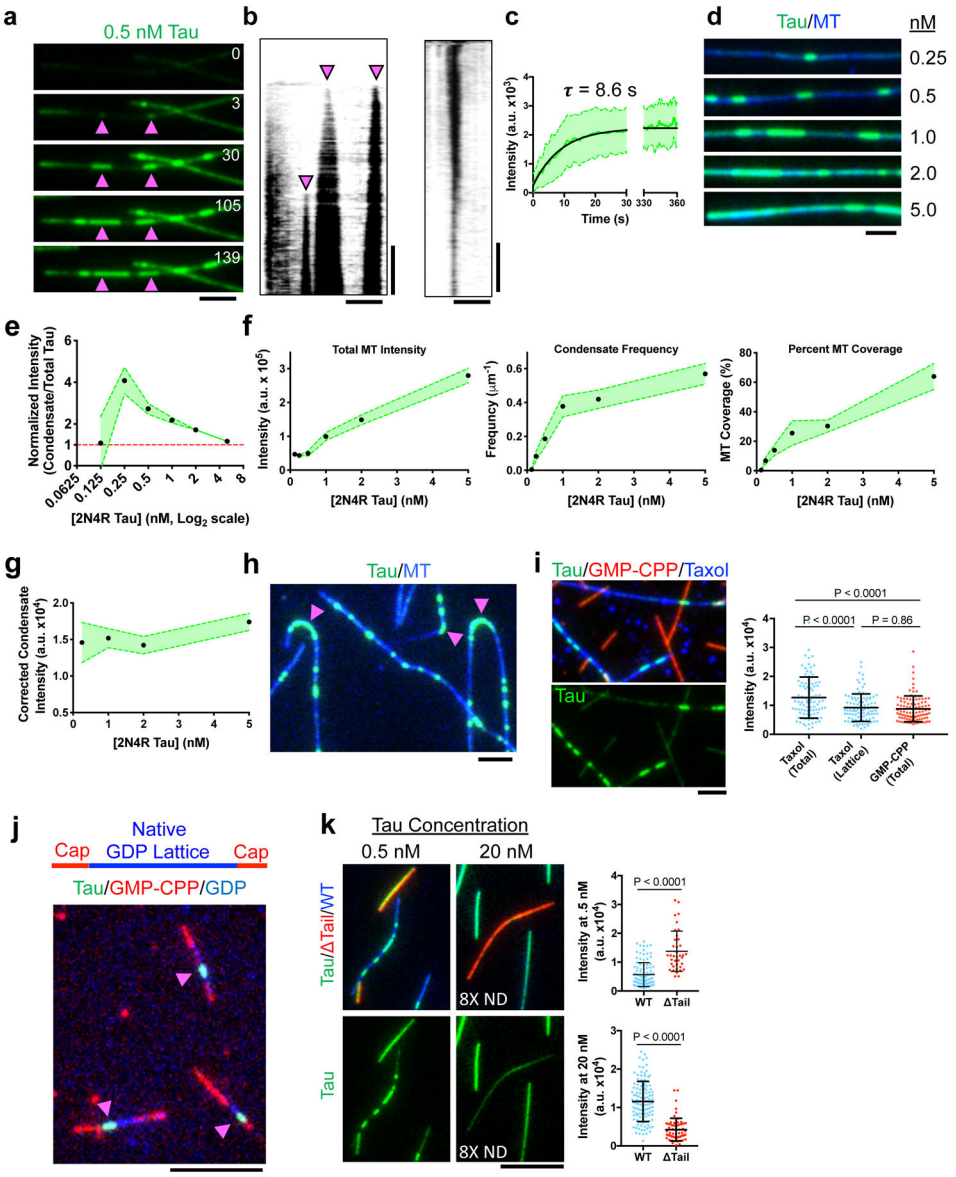

Fig. 1. Microtubules Gate the Spatial Condensation of Tau on the Lattice

a, Time-lapse of tau condensate nucleation and expansion. Arrows denote nucleation sites. Time in sec. N = 4 chambers. **b,** Left: Kymograph of (A). Right: Kymograph of condensate dissolution. N = 2 chambers. **c,** Quantification of tau intensity within condensates over time. Mean ± SD. N = 36 Condensates (3 chambers). **d,** Images of increasing tau concentrations (equal brightness and contrast). N = 3 chambers. **e,** Concentration curve of condensate intensity normalized by total tau intensity. Mean ± 95% CI. N = 4, 52, 144, 233, 275, and 329 condensates (3 chambers each). **f,** Quantification of different parementers of tau concentration titrations. Mean ± 95% CI. N = 77, 100, 104, 111, 100, and 90 MTs. (3 chambers each). **g,** Concentration curve of condensate intensity normalized for increases in tau intensity surrounding condensates. Mean ± 95% CI. N = 52, 233, 275, 329 condensates. (3 chambers each). **h,** Tau accumulation on highly curved regions of microtubules (magenta arrows). N = 3 chambers. **i,** Top: Tau binding to taxol- and GMP-CPP-stabilized MTs.

Below: tau channel. Right: Quantification of tau intensity on taxol- versus GMP-CPP-stabilized MTs. Note total intensity (total) versus intensity outside of condensates (lattice). Mean ± SD. N = 90 (4 chambers), 98 (3 chambers), and 97 (4 chambers) continuous MT segments, respectively. **j,** Tau condensates (green, magenta arrows) on native GDP MT lattice (blue), stabilized at both ends with GMP-CPP caps (red). N = 3 preparations of MTs. **k,** Left: Tau (green) binding to subtilisin-treated (red) and untreated MTs (blue). Below: tau channel. Right: Quantification of tau intensity. Note use of 8X neutral-density (ND) filter for 20 nM tau. Mean ± SD. N = 107 (3 chambers) and 38 (3 chambers) continuous MT segments for 0.5 nM Tau. N = 116 (4 chambers) and 62 (4 chambers) continuous MT segments for 20 nM Tau. For (I) and (K), Student's T-test (two-sided). Scale bars in **a**, **b**, **d**, **h**, **i**: 2 μm, **j**, **k**: 5 μm, **b**: 2 min., 10 min. See Supplementary Figure 1, Supplementary Video 1, and Supplementary Table 1 for source data.

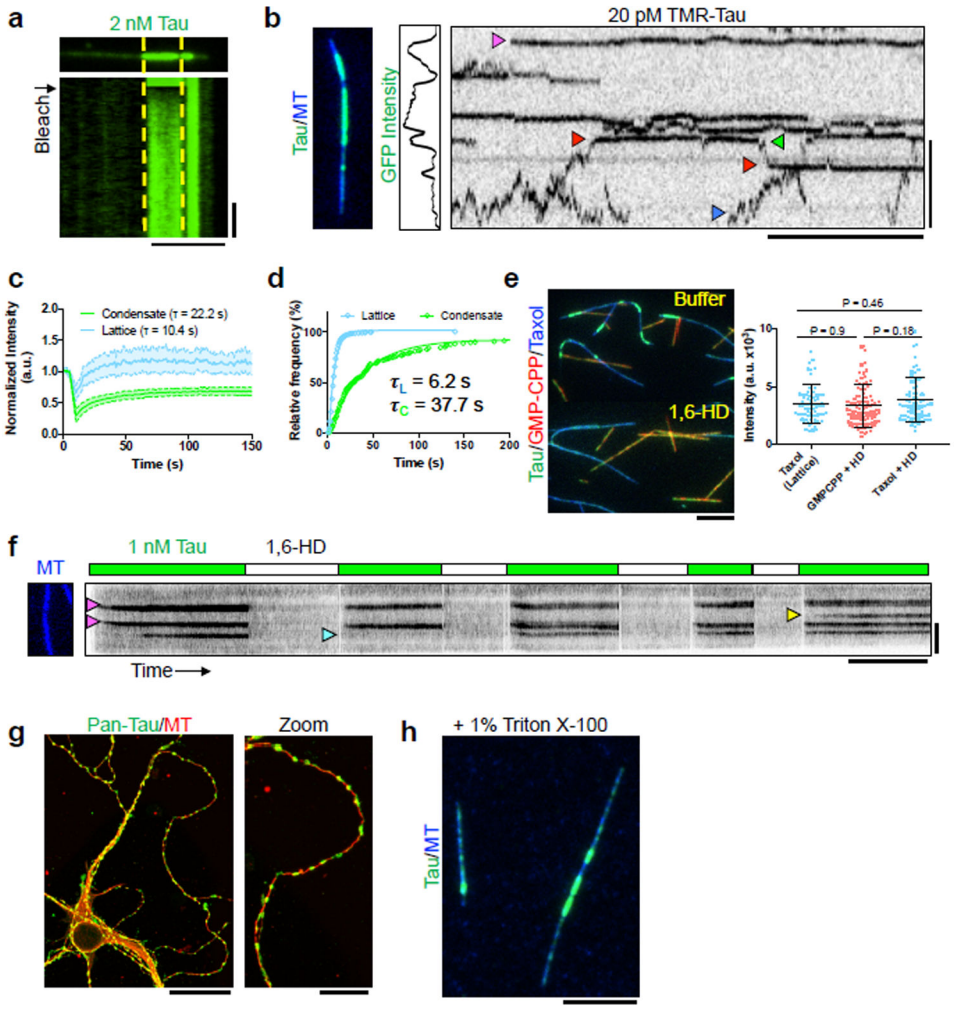

Fig. 2. Tau Condensation Reduces Molecular Dynamics of Tau Molecules on the MT Lattice.

a, Image and kymograph of FRAP of a tau condensate. Yellow lines represent photobleached region. N = 4 chambers. Scale bars: 5 μm, 20 sec. **b,** Quantification of FRAP recovery from both inside and outside (lattice) condensate boundaries. Mean ± SD. N = 24 regions for both condensates and lattice N = 24 segments (4 chambers). Scale bars: 2 μm, 10 sec. **c,** Image, GFP intensity plot, and kymograph of a MT containing GFP-tau condensates and single molecules of SNAP-TMR-labeled tau. Magenta arrow indicates static tau molecule within a condensate. Blue arrow indicates a diffusive molecule outside of a condensate. Red arrow denotes a tau molecule entering, and leaving (green arrow) a condensate. N = 4 chambers. **d,** Cumulative frequency plot of SNAP-TMR-tau dwell times inside and outside (lattice) GFP-tau condensates. N= 451 molecules (3 chambers) and 167 molecules (4 chambers) for lattice and condensates, respectively. **e,** Left: Images of tau (green) bound to taxol- (blue) or GMP-CPP-stabilized (red) MTs before and after addition of 1,6-HD. Tau concentration was kept constant during buffer exchange. Right: Plot of tau intensity outside of condensates (lattice) or total GFP intensity in the presence of 1,6-HD. Mean ± SD. N = 71 (3 chambers), 80 (3 chambers), and 103 (3 chambers) continuous MT segments. Student's t-test (two-sided). Scale bar: 5 μm. **f,** Kymograph of alternating washes

of 1 nM tau with or without 1,6-HD. Alternating buffer exchange scheme diagrammed above, tau concentration was kept constant during buffer exchange. Magenta arrows denote condensate nucleation, blue indicate failure to reform after 1,6-HD washout, yellow indicate new nucleation. N = 2 chambers. Scale bars: 5 μm, 5 min. **g,** Images of immunostained DIV7 mouse hippocampal neurons using the GTX49353 (Genetex) pan-tau antibody. N = 4 preparations of neurons. Scale bars: 25 μm, 10 μm. **h,** Image of *in vitro* tau condensates in the presence of 1% Triton X-100. N = 2 chambers. Scale bar: 5 μm. See Supplementary Figure 2, Supplementary Videos 2-3, and Supplementary Table 1 for source data.

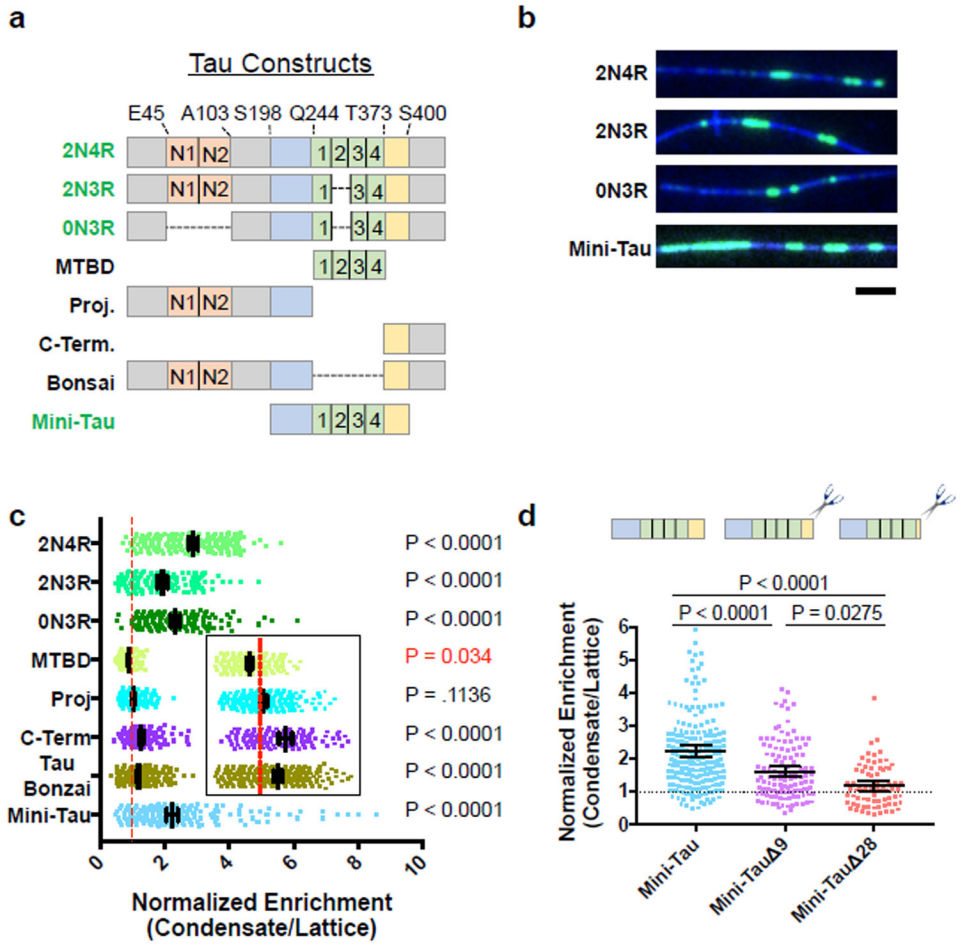

Fig. 3. The C-terminal Pseudo-Repeat Region of Tau Licenses the Rest of the Molecule into Tau Condensates

a, Schematic of natural tau isoforms and constructs used. Orange boxes: alternatively spliced N-term. inserts. Blue: proline-rich domain. Green: MT binding repeats. Yellow: pseudo-repeat domain. Constructs labeled in green text form condensates on their own, those in black text do not. Right, table summarizing ability of the different tau constructs to form condensates. **b,** Images of tau condensates formed from different alternatively spliced or artificially truncated tau constructs. N = 3 chambers each. Scale bar: 2 μm. **c,** Quantification of the fold enrichment of various tau constructs into 2N4R tau condensates versus the MT lattice surrounding the condensate. Inset shows zoom for clarity of MTBD, Proj, C-Term and Tau Bonzai constructs. Right: Statistical significances for enrichment (black) or exclusion (red) of a given GFP-construct within mScarlet-2N4R tau condensates (see Fig.S3). Mean ± 95% CI. N = 211,143, 158, 189, 208, 149, 296, and 239 GFP-2N4R condensates respectively (3-6 chambers for each construct). **d,** Quantification of the fold enrichment of Mini-Tau and C-terminal deletion constructs into 2N4R tau condensates. Data for Mini-Tau reproduced from **c**, for comparison. Mean ± 95% CI. N = 239, 122, and 75 GFP-2N4R condensates respectively (3-4 chambers). For **c,** and **d**, Student's T-test (two-sided). See Supplementary Figure 3 and Supplementary Table 1 for source data.

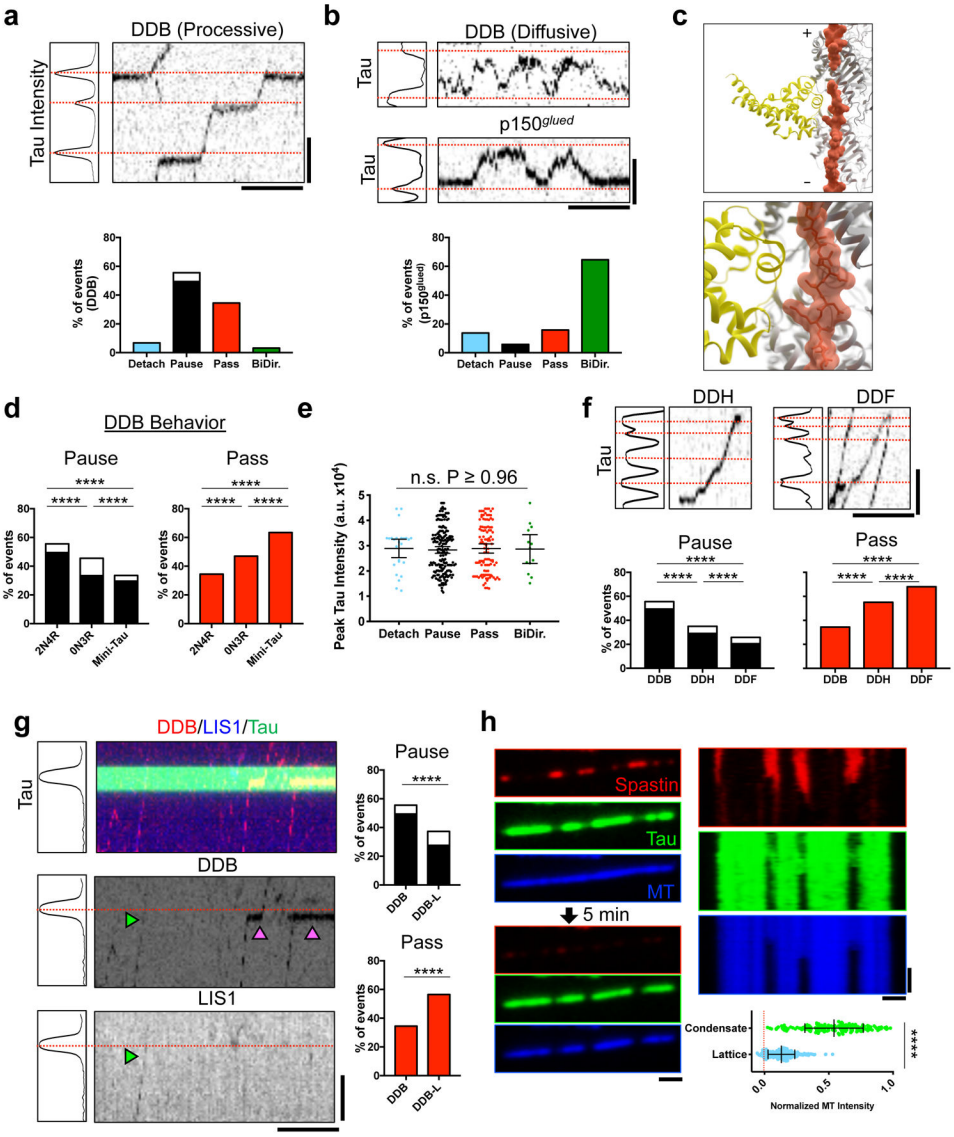

Fig. 4. Tau Condensates Form Selectively Permeable Barriers that Regulate Distinct MT Functions.

a, Top: Plot of tau intensity. Red lines: maximum intensity position (condensates). Right: Kymograph of processive DDB. Bottom: Event distribution for DDB. White indicates proportion that detach during pause. N = 336 events (7 chambers). **b,** Top: Plot of tau intensity with kymograph of diffusive DDB or p150^{glued} molecules. Bottom: Event distribution for p150^{glued}. N = 240 (3 chambers). **c,** Model of tau (R2×4, pdb: 6CVN; orange) and the dynein MTBD (*DYNC1H1*, pdb: 3J1T; yellow) highlighting no steric clash between the two. **d,** Distribution of DDB behaviors at 0N3R or mini-tau condensates. DDB behavior at 2N4R condensates reproduced from **a**. N = 336 events (7 chambers), 226 events (3 chambers), and 399 events (5 chambers) for 2N4R, 0N3R, and mini-tau, respectively. **e,** Peak tau intensity within condensates for each DDB behavior. Mean ± SD. N = 26, 178, 108, and 13 events for each respective behavior (7 chambers). **f,** Top: Plot of tau intensity and kymographs of DDH or DDF behavior. Bottom: Distribution for DDH and DDF behaviors at

condensates. DDB behavior reproduced from **a**. N = 336 events (7 chambers), 268 events (8 chambers), and 697 events (4 chambers) for DDB, DDH, and DDF, respectively. **g,** Left: Plot of tau intensity and kymograph of DDB-L behavior. Right: Passing and pausing distribution for DDB-L. Distribution of DDB behavior reproduced from **a**. Green arrow: DDB-L complex, magenta arrows: DDB complexes. N = 336 events (7 chambers) and 237 events (10 chambers) for DDB and DDB-L, respectively. For **a, f**, and **g** see also Supplementary Figure. 4B. **h,** Left: Images of mScarlet-tau condensates with GFP-spastin before, and after 5 min. incubation. Right: Kymographs from each channel. Magenta arrows: regions of spastin-mediated MT destruction. Bottom: Normalized MT intensity after spastin severing inside/outside condensates. Mean ± SD. N = 228, and 181 continuous MT segments inside and outside condensates (4 chambers), respectively. Student's T-test (two-sided). ****P-value < 0.0001. Scale bars in **a**, **b**, **f**, **g**: 2 μm, 15 sec. **h**: 1 μm, 2 min. See Supplementary Figure 4, Supplementary Videos 4-5, and Supplementary Table 1 for source data.